BEAM
INTERACTIONS
WITH
MATERIALS
AND ATOMS

CrossMark

Nanostructured multielement (TiHfZrNbVTa)N coatings before and after implantation of N+ ions (10^{18} cm^{-2}): Their structure and mechanical properties

A.D. Pogrebnjak [a], O.V. Bondar [a,*], S.O. Borba [a], G. Abadias [b], P. Konarski [c], S.V. Plotnikov [d], V.M. Beresnev [e], L.G. Kassenova [f], P. Drodziel [g]

[a] Sumy State University, Department of Nanoelectronics, 40007, R.-Korsakova 2, Sumy, Ukraine
[b] Institut Pprime, CNRS, Université de Poitiers, ISAE-ENSMA, F86962 Futuroscope Chasseneuil, France
[c] Tele and Radio Research Institute, Ratuszowa 11, 03-450 Warsaw, Poland
[d] D. Serikbaev East-Kazakhstan State Technical University, 070004, Ust-Kamenogorsk, 69 Protozanov St., Kazakhstan
[e] V.N. Karazin Kharkiv National University, 61022, Svobody Sq. 4, Kharkiv, Ukraine
[f] Kazakh University of Economics, Finance and International Trade, St. Zhubanov 7, 010005 Astana, Kazakhstan
[g] Lublin University of Technology, Nadbystrzycka 36, 20-618 Lublin, Poland

ABSTRACT

Multielement high entropy alloy (HEA) nitride (TiHfZrNbVTa)N coatings were deposited by vacuum arc and their structural and mechanical stability after implantation of high doses of N$^+$ ions, 10^{18} cm^{-2}, were investigated. The crystal structure and phase composition were characterized by X-ray diffraction (XRD) and Transmission Electron Microscopy, while depth-resolved nanoindentation tests were used to determine the evolution of hardness and elastic modulus along the implantation depth. XRD patterns show that coatings exhibit a main phase with fcc structure, which preferred orientation varies from (1 1 1) to (2 0 0), depending on the deposition conditions. First-principles calculations reveal that the presence of Nb atoms could favor the formation of solid solution with fcc structure in multielement HEA nitride. TEM results showed that amorphous and nanostructured phases were formed in the implanted coating sub-surface layer (∼100 nm depth). Concentration of nitrogen reached 90 at% in the near-surface layer after implantation, and decreased at higher depth. Nanohardness of the as-deposited coatings varied from 27 to 38 GPa depending on the deposition conditions. Ion implantation led to a significant decrease of the nanohardness to 12 GPa in the implanted region, while it reaches 24 GPa at larger depths. However, the H/E ratio is ⩾0.1 in the sub-surface layer due to N$^+$ implantation, which is expected to have beneficial effect on the wear properties.

© 2016 Elsevier B.V. All rights reserved.

1. Introduction

Ion implantation is among the main methods of surface modification of solids in order to improve their physical-mechanical properties, such as friction, wear, corrosion, adhesion, fatigue strength, biocompatibility etc. [1,2]. It is widely used for semiconductor doping in micro- and nanoelectronics, medicine [3,4], space, chemical and aviation industries [5–9]. The main advantages of ion implantation are preservation of sample sizes, locality (small projective path), high reproducibility, absence of problems with adhesion etc. [7–15]. In order to improve the properties of metals, alloys and ceramics, it is necessary to use high doses of ion implantation, from typically $5 \cdot 10^{16}$ up to 5×10^{17} cm^{-2} [16]. However, in separate cases it is necessary to use an extra high dose of implantation $(1–2) \cdot 10^{18}$ cm^{-2}, which corresponds to the amount of atoms $(1–5) \cdot 10^{23}$ cm^{-3} in implanted volume.

A new class of materials – high-entropy alloys (HEA), which consist of at least 5 atoms with atomic content from 5 to 35 at% – are under great interest nowadays due to their exceptional wealth of physical-mechanical characteristics [8–11,13,12,16–22]. Several works have been performed so far to obtain a comprehensive understanding of the effect of constitutive elements on the microstructure, phase composition and mechanical properties of HEA [23–37]. Nitride coatings from HEA have received particular attention because of improved physical and mechanical characteristics. Most of HEA nitrides consist of 5, 6 or 7 elements, but they can incorporate up to 19 elements [38–45]. The issue of stability of such nitride coatings to oxidation and irradiation

resistance remains still largely unexplored. For the last few years several papers, devoted to the influence of Cu⁻, Au⁻, N⁺ ion implantation on hardness, plasticity index and corrosion resistance were published [46–50]. Improvement of different characteristics, such as hardness, were found in the case of relatively high doses of implantation $(1-2) \cdot 10^{17}$ cm^{-2} [46,49,51–53]. Overview of published studies devoted to the characteristics and properties of HEA nitride coatings shows that improvement of physical-mechanical characteristics is usually obtained in a narrow ion dose range [54,46,55]. However, there are no studies devoted to implantation of high doses of N⁺ ions (up to 10^{18} cm^{-2}), typically when the dose of implanted ions may reach the atomic concentration of the solid material of solid $(1 \times 10^{23} \div 5 \times 10^{23}$ cm$^{-3})$.

The aim of the present work is to explore the microstructure, physical-mechanical properties of nanostructured multielement HEA nitride coatings, implanted by high doses (up to 10^{18} cm^{-2}) of N⁺ ions.

2. Methods

2.1. Experimental procedures

HEA nitride coatings, containing 6 transition metal elements, were produced by cathodic arc evaporation in reactive atmosphere in a Bulat-3T-M device [56]. The employed cathodes consisted of HEA of the Ti-Zr-Hf-V-Nb-Ta system and were produced by vacuum–arc melting in the atmosphere of high purity argon using a nonconsumable electrode into a water-cooled copper vessel. To fabricate a homogeneous composition of the alloy, the ingots were 6–7 times remelted. Coatings were deposited under different working pressures and bias voltages. Deposition parameters and elemental composition of the cathode and nitride coatings are presented in Table 1, where U_b is the bias voltage applied to the substrate and P_N is the nitrogen pressure in the deposition chamber. Steel samples (A 570 Grade 36, the size was $20 \times 20 \times 2$ mm) with polished surfaces were used as substrates.

Ion implantation by N⁺ ions with the energy 60 keV was done on the semi-industrial implanter IMJON (Institute of Fundamental Technological Research, Polish Academy of Sciences, Warsaw, Poland) in vacuum 10^{-3} Pa [7], implantation dose was $\approx 5 \cdot 10^{15}$ cm^{-2} per minute, duration was around 3 h, temperature of the target did not exceed 180 °C, total implantation dose was $1 \cdot 10^{18}$ cm^{-2}.

The elemental composition of the as-deposited and implanted coatings was determined using different chemical analysis methods. We used microanalysis with energy-dispersive spectroscopy (EDS) unit attached to a JEOL-7000F (Japan) scanning electron microscope. Rutherford backscattering spectroscopy (RBS) was used for investigation of the distribution of elements near the surface. Energy of proton beam was 1.5 MeV, energy resolution of the detector was 16 keV. SIMS analysis of the coatings was performed

Table 1
Deposition parameters and concentrations of elements in (TiHfZrVNbTa)N coatings, determined using different chemical analysis methods.

Sample	U_b, V	P_N, Torr	Concentration, at%							Methods of Analysis
			N	Ti	Zr	Hf	V	Nb	Ta	
1	150	3×10^{-3}	54	7.03	8.52	11.30	5.02	9.93	4.20	EDS
2	70	4×10^{-3}	55	10.76	7.71	8.06	5.85	8.38	4.24	
3	150	3×10^{-4}	46	9.04	9.8	12.81	5.60	12.13	4.62	SIMS + EDS
4	150	3×10^{-3}	45.7	9.05	9.85	12.91	5.65	12.18	4.67	EDS
5	150	7×10^{-4}	53	9.72	8.44	9.42	6.54	8.1	4.78	
5[a]	150	7×10^{-4}	44	9	11	12	7	12	5	SIMS + RBS
5[b]	150	7×10^{-4}	46	10	11	9	10	10	4	
Cathode	–	–	–	21.52	18.77	15.5	10.2	18.2	15.81	

[a] concentration before implantation was defined using RBS (integral from the concentration of elements on the whole depth of beam analysis, depth of analysis was 1.06 µm, diameter of the beam was 1 mm).
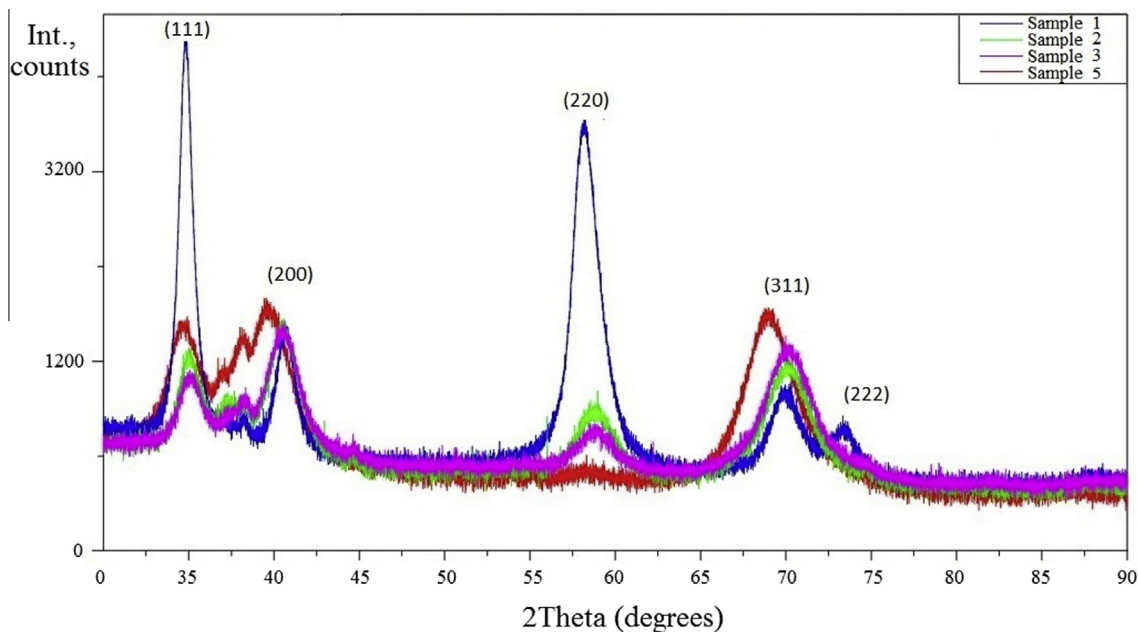[b] concentration after ion implantation.

Fig. 1. XRD patterns of the (TiZrHfVNbTa)N coatings of different samples, deposited by vacuum arc under different N₂ pressures (see Table 1).
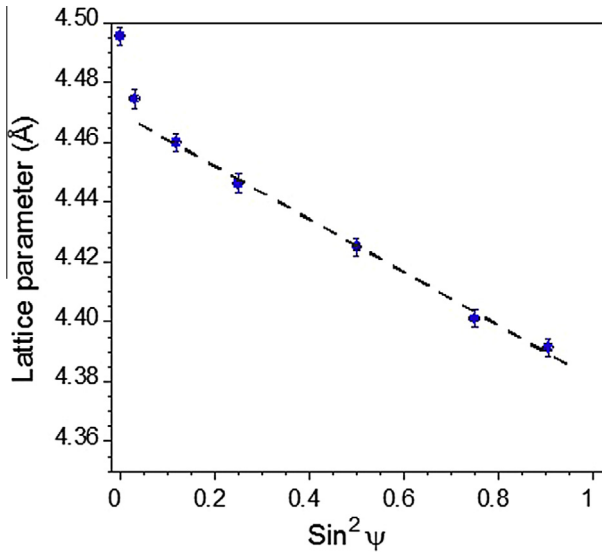
Fig. 2. $\sin^2 \Psi$ plot for the Sample 1 after ion implantation.

on SAJW 05 device, which was equipped with electron bombardment argon ion gun (Physical Electronics) and quadrupole mass analyzer QMA 410 Balzers. Prior to the depth profile analysis, mass spectra were recorded in order to choose certain masses for each analysis. Primary beam scanned the area 2.0×2.0 mm, while secondary ions were collected only from the central part of the crater, which area was around 15% of the total crater's bottom. The diameter of the 5 keV Ar^+ ion beam was around 0.15 mm and incidence angle was 45 degrees. All the obtained results were normalized taking into account RBS data, the depth resolution was about 1 nm.

The crystal structure and phase composition were determined from X-ray diffraction (XRD) performed on a DRON-4 diffractometer operating at 40 kV and 30 mA, using $CuK\alpha$ radiation ($\lambda = 0.154178$ nm) and graphite monochromator as secondary optics. XRD patterns for phase analysis were taken using $\theta-2\theta$ scans with Bragg-Brentano geometry, in the angular range 25–90°, with step $\Delta(2\theta) = 0.02$ [57]. XRD stress analysis was carried out on Sample 1, using the $\sin^2 \Psi$ method [58]. Stress measurements were performed on a four circle Seifert XRD diffractometer, operating at 30 mA and 30 kV, using point focus geometry with Cu X-ray source, a 1.0 mm diameter collimator, a Ni filter to absorb the Cu $K\beta$ wavelength and a scintillation detector
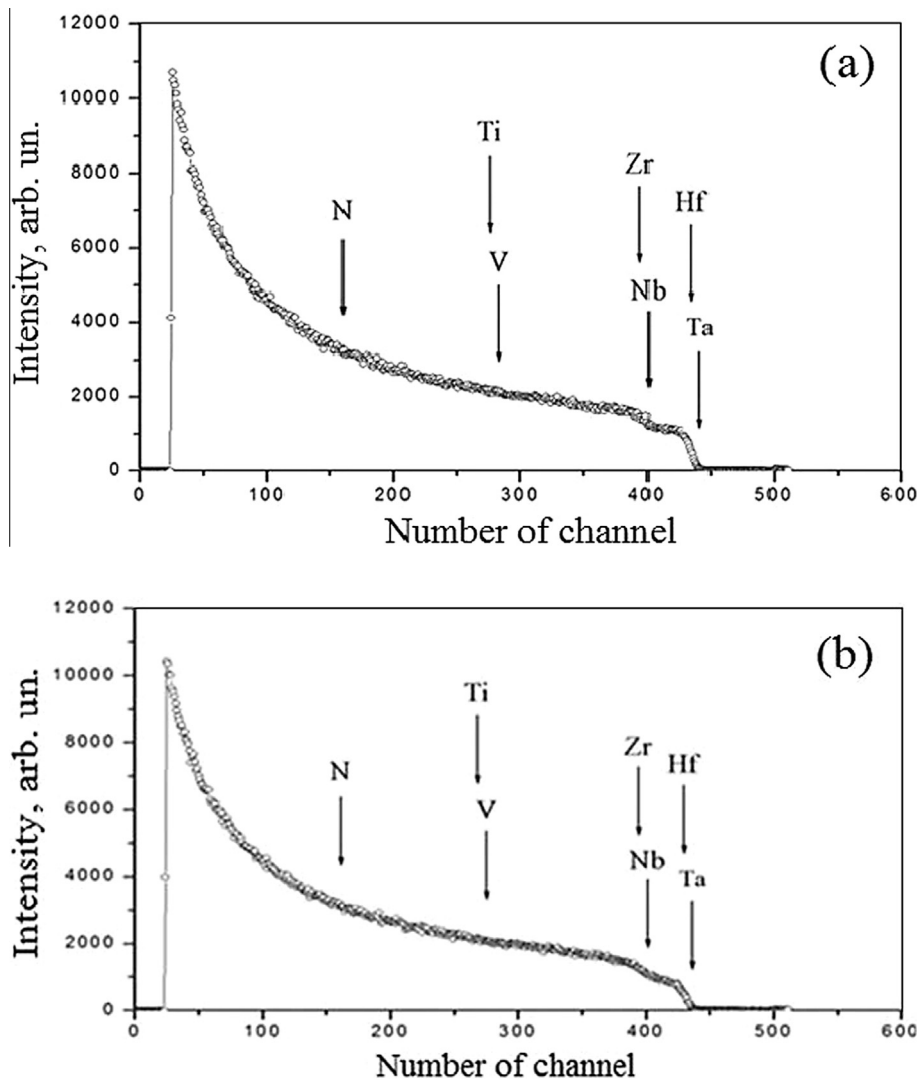

Fig. 3. RBS energy spectra from sample 5: a) before and b) after N^+ ions implantation.
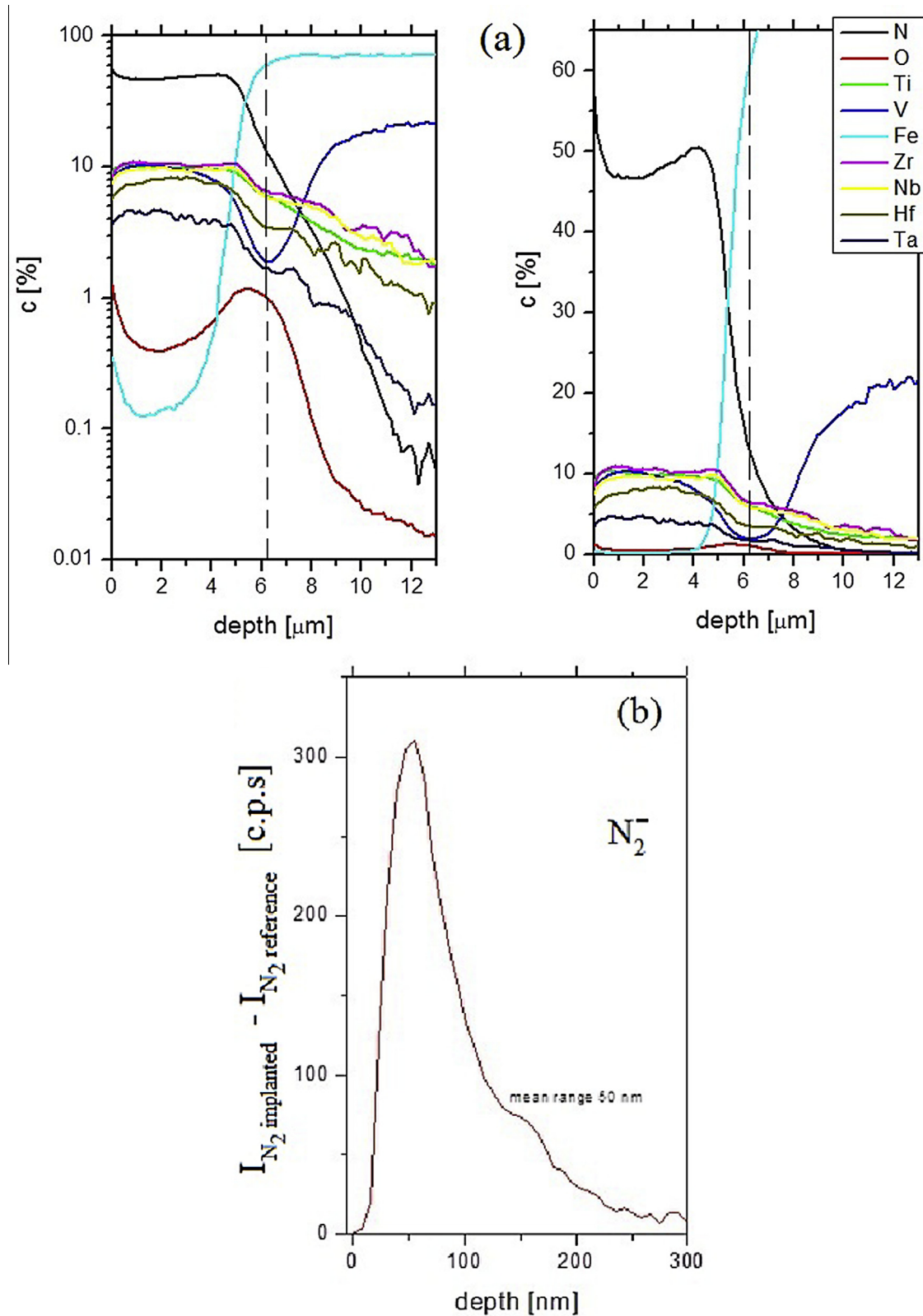
Fig. 4. SIMS depth profile analysis of Sample 3: a) as-deposited coating, normalized data are shown in both linear and logarithmic scale; b) implanted coating, the mean implantation range ~50 nm is obtained from N_2^- secondary ion profile.

[59]. Measurements were taken by recording 2θ scans around the cubic {2 2 0} reflection at different specimen tilt angles Ψ ranging from 0 to 88°.

Complementary investigations of structure and phase composition were done using electron microscope JEOL JEM-2100F, energy of electrons was 200 keV. Thin lamellaes were preliminary prepared using focused ion beam.

Microhardness and elasticity modulus were determined from dynamic nanoindentation of the Berkovich pyramid (Triboindentor TI-950, HYSITRON Inc.). Load on the indenter varied from 500 to

10,000 µN. The values of reduced elastic modulus were obtained using 3-D imaging of the stamp and estimated penetration depth.

2.2. Theoretical methods

First-principles band-structure calculations were carried out using the Quantum-ESPRESSO code [60] for 8-atom cubic supercells of $Ti_{4-n}Nb_nN_4$, $Ti_{4-n}Zr_nN_4$ and $Zr_{4-n}Nb_nN_4$, n = 0,1,2,3,4, representing $Ti_{1-x}Nb_xN$, $Ti_{1-x}Zr_xN$ and $Zr_{1-x}Nb_xN$ alloys, respectively, with the B1 structure (space group Fm-3m, No. 225). Vanderbilt ultra-soft pseudo-potentials were used to describe the electron-ion interaction [61]. The semi-core states were treated as valence states. To describe exchange-correlation energy, the generalized gradient approximation (GGA) of Perdew et al. [62] was employed. The criterion of convergence for the total energy was 10^{-6} Ry/formula unit. To speed up convergence, each eigenvalue was convoluted with a Gaussian with a width of 0.02 Ry. The cut-off energy for the plane-wave basis was set to 38 Ry. The integration in the Brillouin zone (BZ) was done on special **k**-points determined according to the Monkhorst-Pack scheme using a non-shifted mesh (8 8 8). All initial structures were optimized by simultaneously relaxing the supercell basis vectors and the atomic positions inside the supercell using the Broyden–Fletcher–Goldfarb–Shanno (BFGS) algorithm [63]. The relaxation of the atomic coordinates and of the supercell was considered to be complete when atomic forces were less than 1.0 mRy/Bohr (25.7 meV/Å), stresses were smaller than 0.05 GPa, and the total energy during the structural optimization iterative process was changing by less than 0.1 mRy (1.36 meV). To estimate the formation energies of the nitrides under consideration, the total energies of the Ti, Zr and Nb crystal as well as the N_2 gas molecule were calculated.

3. Results and discussion

3.1. Structural and chemical investigation

It can be seen from Table 1, that increasing of P_N from 3×10^{-4} to 3×10^{-3} Torr led to increasing of nitrogen concentration in the coating, while the content of metallic elements, such as Ti, Nb, V decreased. Changes of pressure in the deposition chamber also led to changes in concentrations of elements in the coatings, they differed from the cathode composition.

Fig. 1 displays XRD patterns of the as-deposited coatings under different P_N pressures in the deposition chamber. It can be seen that the main phase formed consists in a fcc crystal lattice, which is commonly reported for such HEA nitrides. Using Scherrer formula, the mean size of crystallites of fcc-phase in the coatings was estimated to be 8 nm at low P_N. The preferred orientation of crystallites growth with the plane (2 0 0), parallel to the surface, was formed at low P_N. These coatings demonstrated high hardness up to 38 ± 0.7 GPa in according to hardness measurements using Vickers method. The XRD pattern from sample 1 (Fig. 1) deposited under comparatively high pressure 4×10^{-3} Torr reveals that the preferred orientation changed to [1 1 1], but a significant fraction of [1 1 0]-oriented crystallites is also found. The mean size of crystallites, extracted from 1 1 1 peak width, increased to 17–20 nm at high P_N. These values are in fairly good agreement with the results of the HRTEM analysis, as will be discussed further below.

Fig. 2 shows the evolution of the lattice parameter of crystallites with fcc structure, after ion implantation of sample 1, as a function of $\sin^2\Psi$. A linear variation is observed in the angular Ψ range of 20–72°, with a negative slope indicative of the presence of compressive stress. The deviation from linearity at low $\sin^2\Psi$ values can reflect the presence of stress gradients along the film depth or a more complex stress state due to the presence of neighboring interacting crystallites with hexagonal structure (see TEM analysis in Figs. 7 and 8). The stress analysis was performed assuming a macroscopically (elastically) isotropic specimen, subjected to a rotationally symmetric in-plane biaxial stress state, $\sigma_1 = \sigma_2 = \sigma$. For a cubic material, the strain-stress relation is given by

$$\varepsilon_{hkl} = \frac{a_{hkl} - a_0}{a_0} = \left(2S_1^{hkl} + \frac{1}{2}S_2^{hkl}\sin^2\psi\right)\sigma$$

where S_1^{hkl} and S_2^{hkl} are the so-called X-ray elastic constants (XECs) for the {hkl} reflections employed in the diffraction measurements, and a_0 is the stress-free lattice parameter. The XECs differ from the mechanical elastic constants, $S_1^{mech} = -\frac{\nu}{E}$ and $S_2^{mech} = \frac{2(1+\nu)}{E}$, usually employed to describe the behavior of isotropic polycrystalline aggregates, where E is the Young modulus and ν the Poisson ratio. In the present analysis, the XECs were calculated for the {2 2 0}
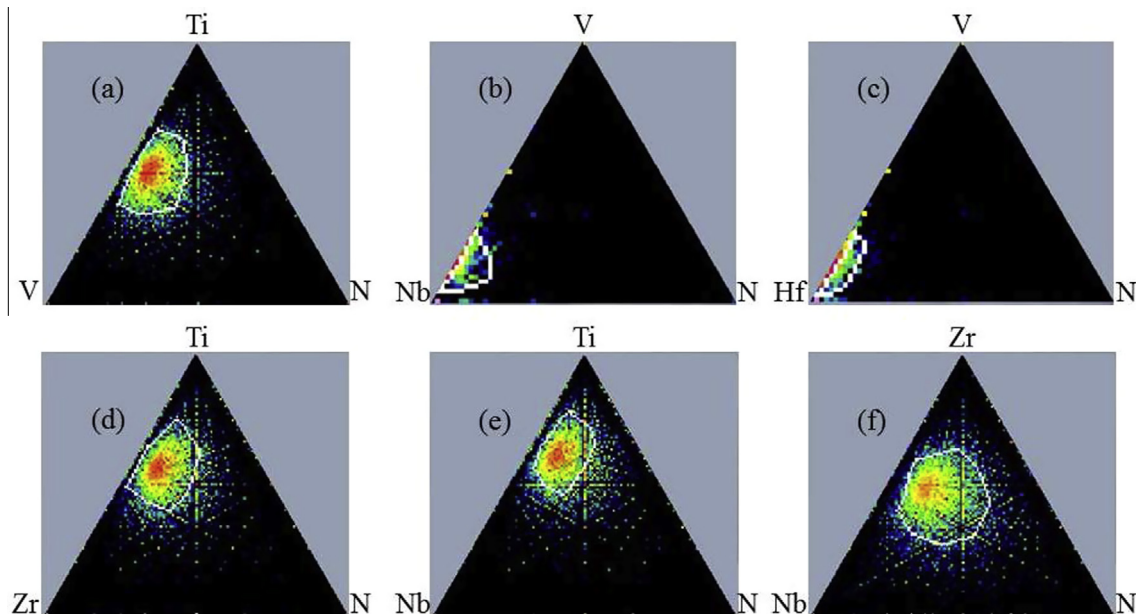

Fig. 5. Triangle map of elemental distribution, obtained from EDS: a) in the V–Ti–N solid solution; b) Nb–V–N solid solution; c) Hf–V–N solid solution; d) Ti–Zr–N solid solution; e) Ti–Nb–N solid solution; f) Zr–Nb–N solid solution.
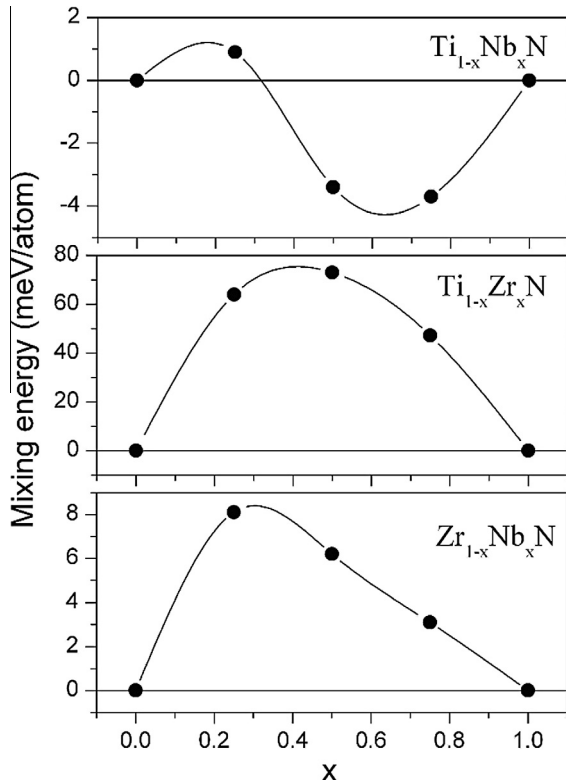
Fig. 6. Computed mixing energy (E_{mix}) of $Ti_{1-x}Nb_xN$, $Ti_{1-x}Zr_xN$ and $Zr_{1-x}Nb_xN$ alloys as a function of composition x.
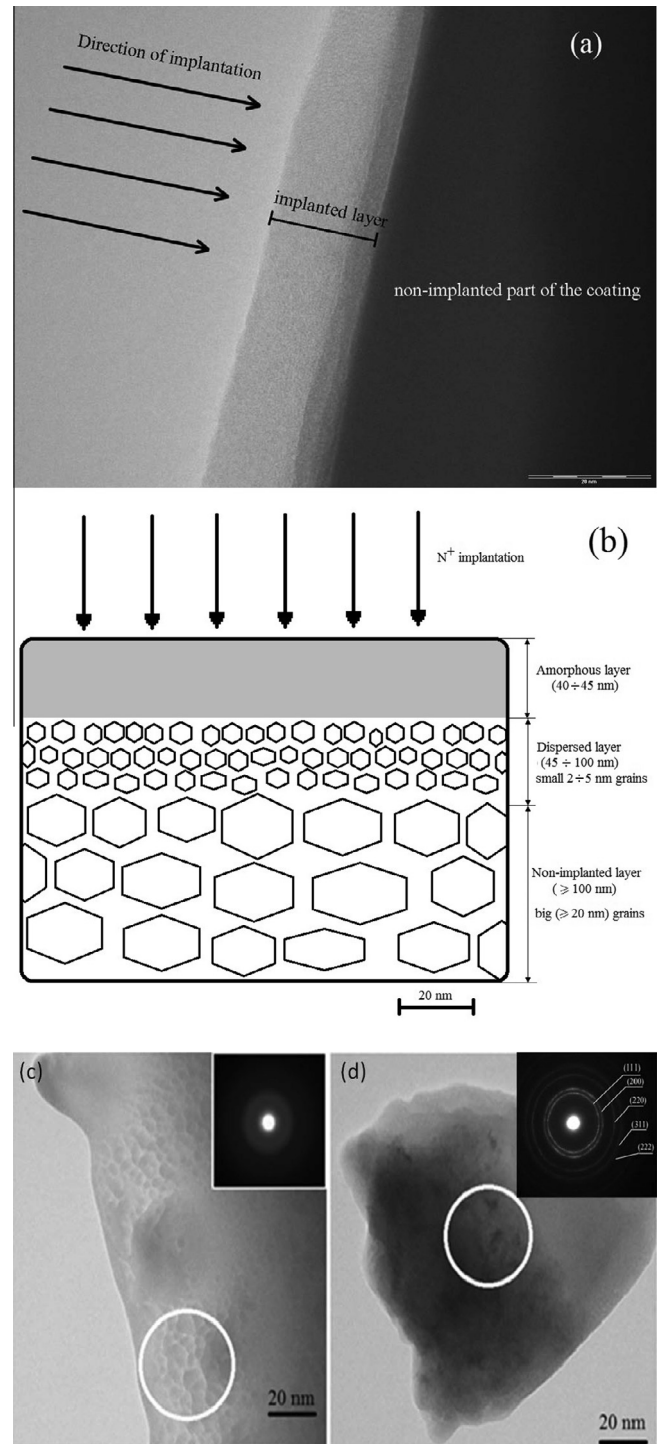

Fig. 7. TEM images of implanted coating's cross-section (Sample 2): a) general view of the implanted sample; b) schematic view of the implanted sample showing the direction of implantation, the implanted region consisting of an amorphous near-surface layer and a dispersed layer with small nanograins (~5 nm in size), and the non-implanted layer at higher depth with much larger nanograins (⩾20 nm), c) near-surface layer of amorphous phase, d) the nanocrystalline layer below amorphous layer; corresponding SAED patterns are shown in the inserts.

reflection assuming a Reuss model (i.e. equal stress state for all crystallites; see Appendix A of [58] for the detailed expressions). As no elastic data have been reported for such multielement HEA nitride compound, the C_{ij} values were rather extrapolated from a rule of mixture based on the available C_{ij} data of the literature for binary compounds [59,64]. The following values were employed: C_{11} = 594 GPa, C_{12} = 132 GPa, and C_{44} = 112 GPa. This yields σ = −5.1 ± 0.2 GPa and a_0 = 4.428 ± 0.003 Å. The relative large compressive stress level is typical for nitride coating deposited by vacuum arc [56].

Results of RBS analysis of as-deposited and implanted coatings (Sample 5) are presented on Fig. 3a and b. A sharp "ledge" is observed between Ti, Zr, V, Nb from the one side and Ta, Hf elements from the other side in the Fig. 3a. Stoichiometry had changed throughout the whole depth of the analysis for implanted coatings. A fit of the RBS spectra using SIMNRA yields a value of $(TiVZrNb)_{0.39}/(TaHf)_{0.17}$ ratio in the as-deposited coatings and $(TiVZrNb)_{0.41}/(TaHf)_{0.13}$ after ion implantation. Moreover, we can see a bluring of the "ledge" on the RBS spectrum in the channel range (400 ÷ 440) in Fig. 3a in comparison with the channel range (390 ÷ 425) in Fig. 3b due to the processes of atomic collisions, formation of collision cascades, ion mixing and accelerated radiation diffusion. We should point, that for calculation of the projective path of the N^+ ions we used standard software [65–67], but it was very hard to calculate profiles of N^+ ions due to quite high roughness of the coating's surfaces after vacuum-arc deposition. Nevertheless, we could conclude that the elemental concentration was homogeneous along the thickness of the as-deposited coating. Ion implantation led to partial sputtering of the surface layer, concentration of N^+ ions increased up to 90 at%. Taking into account the results of SIMS analysis, presented below in Fig. 4, we can state, that N^+ concentration reached 90 at%, the remaining part of N^+ ions was engaged in the process of volatilization of the near-surface layer.

The results of SIMS analysis of the Sample 3 are presented in Fig. 4. The analysis shows the entire thickness of the coating from the top to the substrate, total thickness of the coating is around 6.3 μm, as seen from the Fig. 4a. In order to extract nitrogen depth profiles, additional analyses were performed. We detected positive ion currents of selected masses: 14 Au and 28 Au, corresponding to

N and N_2 positive and negative secondary ions. Since nitrogen was implanted into a host nitride structure, we subtracted secondary ion plots of not implanted structure from the plots of the implanted structure. Such a procedure allows estimating the amount of the implanted nitrogen, see Fig. 4b. Obtained results show, that the mean implantation range (~50 nm) is lower than that the value of 68–72 nm calculated from the projective path of N^+ ions with energy 60 keV. The closest result is for negative secondary ions N_2 (50 nm mean implantation range). The reason of this discrepancy can be due to assumption, that sputtering rate is constant across the whole structure. If we consider that the sputtering rate within the implantation range is higher than across the whole structure, we would get better correlation to the expected values of mean implantation ranges.

3.2. Influence of ion implantation on phase stability

A convenient way to illustrate the elemental composition of multielement HEA nitrides is to get use of the Gibbs-Rosenbaum triangle representation, for different combination of constitutive elements of ternary sub-systems, as shown in Fig. 5 for the case of Sample 2. The vertices of an equilateral triangle correspond to the 100% content of each element in the system. The method of

defining the composition was suggested by Gibbs, and it is based on the fact, that the sum of perpendiculars from any point within an equilateral triangle on each side is equal to the height of the triangle. Rosenbaum suggested using the three segments of straight lines parallel to the sides of the triangle and extending from this point to the intersection with each of the sides of the triangle. The sum of three line segments for each point within an equilateral triangle is equal to the length of its sides. For total composition of the system we marked the percentage of each component in the way, when each peak of the triangle corresponds to 100% content of the appropriate component. From the Fig. 5 we can see that percentage content of the Nb-N, Ti-N and Hf-N systems is noticeably higher than of the V-N and Zr-N, thus it leads to forming of solid solution with high content of NbN and HfN. Forming of stable solid solution confirms the effect of influence of high entropy of mixing on forming of the crystal lattice.

The Gibbs free energy of mixing of the alloys under investigation, calculated at T = 0 K (i.e., formation energy), is presented in the Fig. 6 as a function of composition x. The positive formation energy implies that the $Ti_{1-x}Zr_xN$ alloys are not stable, and will decompose into TiN and ZrN with the chemical driving force (E_{mix}). However, all alloys can be stabilized in some range of composition, depending on temperature, since the configurational entropy is
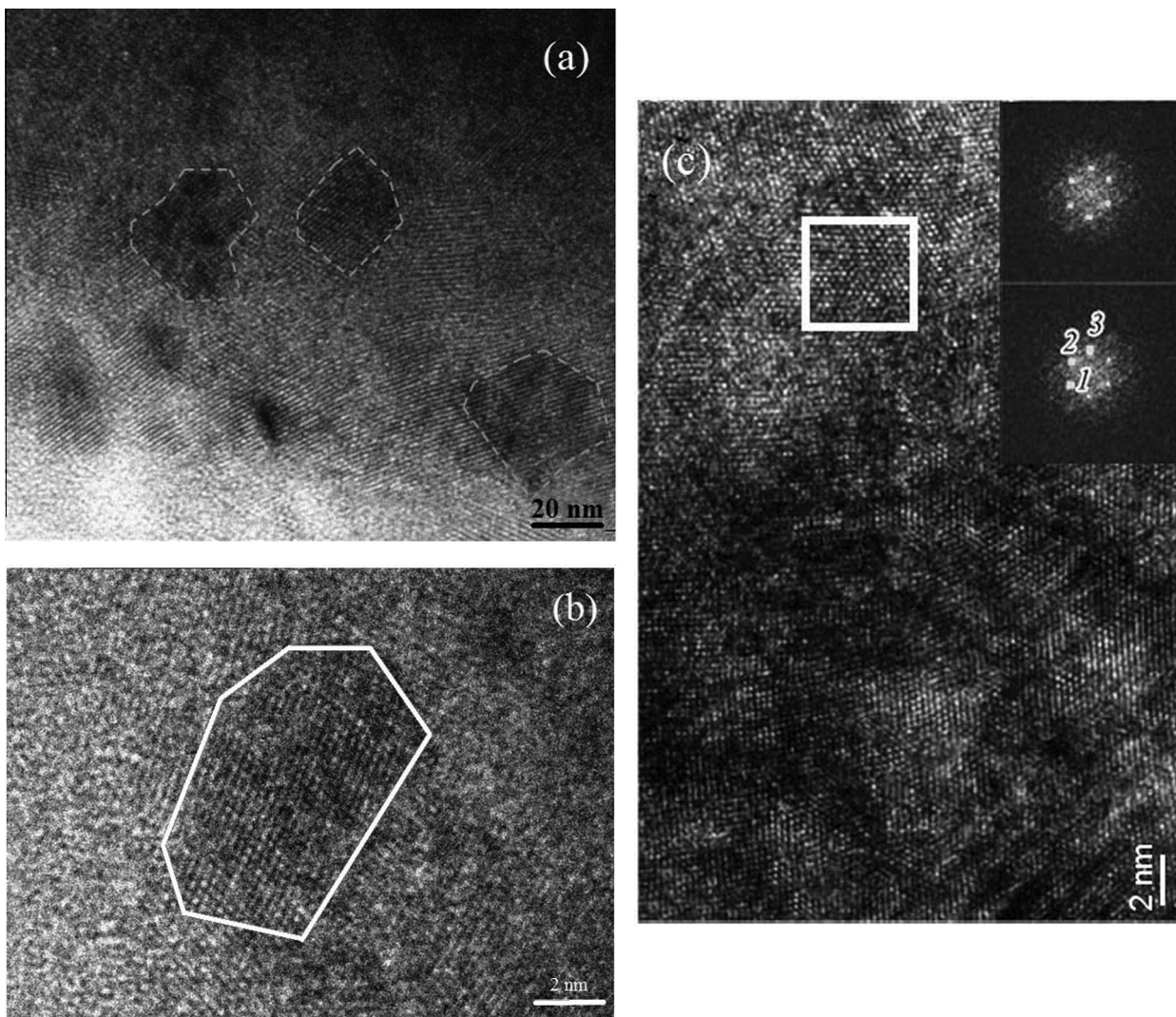

Fig. 8. TEM images of the cross-sections of the (Ti-Zr-Hf-V-Nb-Ta)N coatings from Sample 4: a) near-surface layer (scale bar is 20 nm); b) magnification of region c) showing a nanocrystal (scale bar is 2 nm); c) HR-TEM image of the nanocrystalline region at a depth of 180 nm; corresponding FFT patterns are shown in the insert.
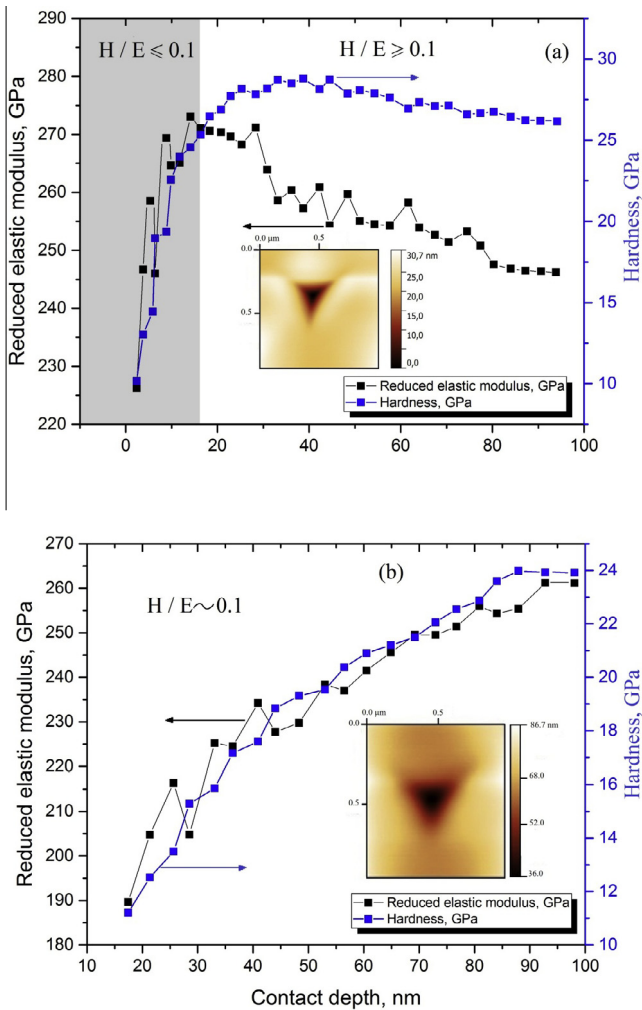
Fig. 9. Depth profile of hardness and elastic modulus for Sample 5: a) as-deposited coating, b) implanted coating.

always positive and promotes a decrease in Gibbs free energy. Since the values of E_{mix} for $Ti_{1-x}Nb_xN$ and $Zr_{1-x}Nb_xN$ are very small and some of them are negative, these alloys can be stabilized as solid solutions at moderate temperatures. These findings confirm the possibility of the formation of fcc solid solutions based on TiN, ZrN and NbN in thin films. Since in our films we observed only solid solutions based on these nitrides, one can suppose that the presence of NbN in the films precludes the separation of TiN and ZrN from the $Ti_{1-x}Zr_xN$ alloys.

After ion implantation, modification of the coating microstructure is essentially concentrated in the sub-surface layer (100 nm thick), as evidenced from TEM (Fig. 7a). A schematic illustration of the depth-dependent coating microstructure after ion implantation is provided in Fig. 7b. As we can see from TEM investigations on sample 5 (Fig. 7c), an amorphous layer with thickness of ∼40 nm is formed. A nanocrystalline layer with nanocrystals of the size 5–6 nm is located under this amorphous layer. Phase analysis of this layer showed the presence of fcc phase, based on solid solution, in which Ti, Hf, Zr, V, Nb, Ta were randomly distributed in sub-lattice. A higher magnification of the nanocrystalline layer is shown in Fig. 8, where nanograins with typical size of 5–6 nm are clearly distinguishable (Fig. 8a). Lattice planes are clearly resolved and their boundaries are marked with white lines. The interplanar spacings, extracted from SAED patterns of Fig. 7d, are equal to 0.235 nm and 0.158 nm, and correspond to (2 0 0) and

(2 2 0) planes of fcc structure. In addition, we can see increasing of the interplanar spacing to 0.255–0.259 nm −(1 1 1) plane and 0.226 nm (plane (2 0 0)) far from the surface of the nanostructured coating (not shown here). Such values are close to the values determined from XRD data. Reflections with 0.275–0.278 nm interplanar spacing can be seen at the depth of 180 nm (Fig. 8c). It is known, that fcc and hcp lattices are quite similar in their internal energy with small enough energy barrier for transformation. Interplanar spacing of 0.275–0.278 corresponds to (1 0 0) plane for nitrides of transition metals with hcp lattice. Therefore, it can be assumed, that in local regions of the coating lattice transformation from fcc to hcp can occur by a shear mechanism due to composition inhomogeneity associated with relatively low nitrogen content (low working pressure during deposition). The driving force of this process is the great thermodynamic stability of the hcp lattice with a deficiency of nitrogen atoms in the octahedral interstices.

3.3. Influence of ion implantation on mechanical properties

Results of nanoindentation measurements of hardness and reduced elastic modulus of the Sample 5 before and after ion implantation are presented in Fig. 9a and b respectively. It is possible to estimate the indenter penetration depth from the traces of the indenter on the inserts. Hardness and reduced elastic modulus of the as-deposited sample sharply increased near the surface at the depth up to 18 nm, but the H/E ratio remained less or equal to 0.1 for this depth, thus the coating can be considered as fragile. The values of hardness and reduced elastic modulus slowly decreased with the penetration depth increasing, and finally were set to the values 26.5 GPa and 247 GPa accordingly. For this area the H/E ratio became greater or equal to 0.1. However, indentation of the implanted sample showed, that values of hardness and reduced elastic modulus increased smoothly with the penetration depth increasing and reached their maximum values 24 GPa and 260 GPa accordingly at the maximum penetration depth of 100 nm. H/E ratio remained around 0.1, which indicates a good plasticity of the implanted coating. Such dependencies of hardness and reduced elastic modulus can be explained by the fact, that amorphous layer was formed in the near-the-surface region after implantation of high doses of N+ ions, see Fig. 7b. Hardness of the amorphous layer is lower than of crystalline layer. Scratch-tests results (not reported here) of the investigated coatings before and after implantation had also demonstrated decreasing of the friction coefficient in implanted zone.

4. Conclusions

Implantation of very high doses of N^+ ions (10^{18} cm^{-2}) with 60 keV energy into (TiHfZrNbVTa)N coatings deposited by vacuum arc result in an modification of the microstructure up to 100 nm depth. The deposited coatings exhibit a main fcc structure. The implanted region consists of an amorphous near-surface layer (40 nm in depth) and a nanocrystalline layer (50–100 nm in depth). Hardness decreased to 12 GPa in the near-the-surface layers and increased with penetration depth to its maximum values 24 GPa. Increasing of the pressure in the deposition chamber up to 3×10^{-3} Torr led to significant increasing of nitrogen concentration (8 at%) in the coating, as well as to decreasing of the content of Ti, V, Nb metals. Changes in pressure led to appearing of preferred orientation of the plane (1 1 1), parallel to the plane of growth, and to forming of hcp lattice locally. Plasticity index H/E increased and exceed the value of 0.1, thus we can state, that fabricated coatings have good wear resistance, as it was confirmed by preliminary scratch-tests.

Acknowledgements

References

[1] Y. Zhao, S.M. Wong, H.M. Wong, S. Wu, T. Hu, K.W.K. Yeung, P.K. Chu, Effects of carbon and nitrogen plasma immersion ion implantation on in vitro and in vivo biocompatibility of titanium alloys, ACS Appl. Mater. Interfaces 5 (2013) 1510–1516, http://dx.doi.org/10.1021/am302961h.

[2] K.W.K. Yeung, R.Y.L. Chan, K.O. Lam, S.L. Wu, X.M. Liu, C.Y. Chung, P.K. Chu, W. W. Lu, D. Chan, K.D.K. Luk, K.M.C. Cheung, In vitro and in vivo characterization of novel plasma treated nickel titanium shape memory alloy for orthopedic implantation, Surf. Coatings Technol. 202 (2007) 1247–1251, http://dx.doi.org/10.1016/j.surfcoat.2007.07.093.

[3] S. Mändl, B. Rauschenbach, Improving the biocompatibility of medical implants with plasma immersion ion implantation, Surf. Coatings Technol. 156 (2002) 276–283, http://dx.doi.org/10.1016/S0257-8972(02)00085-3.

[4] P.A. Dearnley, A review of metallic, ceramic and surface-treated metals used for bearing surfaces in human joint replacements, Proc. Inst. Mech. Eng. Part H 213 (1999) 107–135, http://dx.doi.org/10.1243/0954411991534843.

[5] V.I. Lavrentiev, A.D. Pogrebnjak, High-dose ion implantation into metals, Surf. Coatings Technol. 99 (1998) 24–32, http://dx.doi.org/10.1016/S0257-8972(97) 00122-9.

[6] N.A.P.K. Kumar, C. Li, K.J. Leonard, H. Bei, S.J. Zinkle, Microstructural stability and mechanical behavior of FeNiMnCr high entropy alloy under ion irradiation, 113 (2016) 230–244. doi:10.1016/j.actamat.2016.05.007.

[7] A.D. Pogrebnjak, S.N. Bratushka, V.M. Beresnev, N. Levintant-Zayonts, Shape memory effect and superelasticity of titanium nickelide alloys implanted with high ion doses, Russ. Chem. Rev. 82 (2013) 1135–1159, http://dx.doi.org/10.1070/RC2013v082n12ABEH004344.

[8] O.N. Senkov, S.V. Senkova, D.B. Miracle, C. Woodward, Mechanical properties of low-density, refractory multi-principal element alloys of the Cr–Nb–Ti–V–Zr system, Mater. Sci. Eng., A 565 (2013) 51–62, http://dx.doi.org/10.1016/j.msea.2012.12.018.

[9] N.D. Stepanov, D.G. Shaysultanov, G.A. Salishchev, M.A. Tikhonovsky, E.E. Oleynik, A.S. Tortika, O.N. Senkov, Effect of V content on microstructure and mechanical properties of the CoCrFeMnNiVx high entropy alloys, J. Alloys Compd. 628 (2015) 170–185, http://dx.doi.org/10.1016/j.jallcom.2014. 12.157.

[10] V. Braic, A. Vladescu, M. Balaceanu, C.R. Luculescu, M. Braic, Nanostructured multi-element (TiZrNbHfTa)N and (TiZrNbHfTa)C hard coatings, Surf. Coatings Technol. 211 (2012) 117–121, http://dx.doi.org/10.1016/j.surfcoat.2011. 09.033.

[11] D.-C. Tsai, Y.-L. Huang, S.-R. Lin, S.-C. Liang, F.-S. Shieu, Effect of nitrogen flow ratios on the structure and mechanical properties of (TiVCrZrY)N coatings prepared by reactive magnetron sputtering, Appl. Surf. Sci. 257 (2010) 1361–1367, http://dx.doi.org/10.1016/j.apsusc.2010.08.078.

[12] A.D. Pogrebnjak, A.A. Bagdasaryan, I.V. Yakushchenko, V.M. Beresnev, The structure and properties of high-entropy alloys and nitride coatings based on them, Russ. Chem. Rev. 83 (2014) 1027–1061, http://dx.doi.org/10.1070/RCR4407.

[13] A. Munitz, S. Salhov, S. Hayun, N. Frage, Heat treatment impacts the microstructure and mechanical properties of AlCoCrFeNi high entropy alloy 683 (2016) 221–230, http://dx.doi.org/10.1016/j.jallcom.2016.05.034.

[14] S. Kucharski, J. Luckner, Mechanical response of nitrogen ion implanted NiTi shape memory alloy, Mater. Des. 56 (2014) 671–679, http://dx.doi.org/10.1016/j.matdes.2013.11.056.

[15] K. Takeda, R. Matsui, H. Tobushi, S. Homma, N. Levintant-Zayonts, S. Kucharski, Enhancement of bending fatigue life in TiNi shape-memory alloy tape by nitrogen ion implantation, Arch. Mech. 67 (2015) 293–310.

[16] A.D. Pogrebnjak, A.M. Tolopa, A review of high-dose implantation and production of ion mixed structures, Nucl. Instrum. Methods Phys. Res. Sect. B 52 (1990) 25–43, http://dx.doi.org/10.1016/0168-583X(90)90598-O.

[17] T.M. Butler, M.L. Weaver, Oxidation behavior of arc melted AlCoCrFeNi multicomponent high-entropy alloys, 674 (2016) 229–244. doi:10.1016/j.jallcom.2016.02.257.

[18] G. Dirras, L. Lilensten, P. Djemia, M. Laurent-Brocq, D. Tingaud, J.P. Couzinié, L. Perrière, T. Chauveau, I. Guillot, Elastic and plastic properties of as-cast equimolar TiHfZrTaNb high-entropy alloy, 654 (2016) 30–38. doi:10.1016/j.msea.2015.12.017.

[19] N.N. Guo, L. Wang, L.S. Luo, X.Z. Li, R.R. Chen, Y.Q. Su, J.J. Guo, H.Z. Fu, Hot deformation characteristics and dynamic recrystallization of the MoNbHfZrTi refractory high-entropy alloy, 651 (2016) 698–707. doi:10.1016/j.msea.2015.10.113.

[20] C. Li, Y. Xue, M. Hua, T. Cao, L. Ma, L. Wang, Microstructure and mechanical properties of AlxSi0.2CrFeCoNiCu1-x high-entropy alloys, 90 (2016) 601–609. doi:10.1016/j.matdes.2015.11.013.

[21] A. Poulia, E. Georgatis, A. Lekatou, A.E. Karantzalis, Microstructure and wear behavior of a refractory high entropy alloy, 57 (2016) 50–63. doi:10.1016/j.ijrmhm.2016.02.006.

[22] Rogal, F. Czerwinski, P.T. Jochym, L. Litynska-Dobrzynska, Microstructure and mechanical properties of the novel Hf25Sc25Ti25Zr25 equiatomic alloy with hexagonal solid solutions, 92 (2016) 8–17. doi:10.1016/j.matdes.2015.11.104.

[23] N.N. Guo, L. Wang, L.S. Luo, X.Z. Li, R.R. Chen, Y.Q. Su, J.J. Guo, H.Z. Fu, Effect of composing element on microstructure and mechanical properties in Mo-Nb-Hf-Zr-Ti multi-principle component alloys, 69 (2016) 13–20. doi:10.1016/j.intermet.2015.10.011.

[24] C.C. Juan, K.K. Tseng, W.L. Hsu, M.H. Tsai, C.W. Tsai, C.M. Lin, S.K. Chen, S.J. Lin, J.W. Yeh, Solution strengthening of ductile refractory HfMoxNbTaTiZr high-entropy alloys, 175 (2016) 284–287. doi:10.1016/j.matlet.2016.03.133.

[25] M. Laurent-Brocq, L. Perrière, R. Pirès, Y. Champion, From high entropy alloys to diluted multi-component alloys: range of existence of a solid-solution, 103 (2016) 84–89. doi:10.1016/j.matdes.2016.04.046.

[26] F. Salemi, M.H. Abbasi, F. Karimzadeh, Synthesis and thermodynamic analysis of nanostructured CuNiCoZnAl high entropy alloy produced by mechanical alloying, 685 (2016) 278–286. doi:10.1016/j.jallcom.2016.05.274.

[27] H. Song, F. Tian, D. Wang, Thermodynamic properties of refractory high entropy alloys, 682 (2016) 773–777. doi:10.1016/j.jallcom.2016.04.320.

[28] S. Syed Ghazi, K.R. Ravi, Phase-evolution in high entropy alloys: role of synthesis route, 73 (2016) 40–42. doi:10.1016/j.intermet.2016.03.002.

[29] Z. Wang, I. Baker, Interstitial strengthening of a f.c.c. FeNiMnAlCr high entropy alloy, 180 (2016) 153–156. doi:10.1016/j.matlet.2016.05.122.

[30] Z. Wang, M. Wu, Z. Cai, S. Chen, I. Baker, Effect of Ti content on the microstructure and mechanical behavior of (Fe36Ni18Mn33Al13)100-xTix high entropy alloys, 75 (2016) 79–87. doi:10.1016/j.intermet.2016.06.001.

[31] P. Wilson, R. Field, M. Kaufman, The use of diffusion multiples to examine the compositional dependence of phase stability and hardness of the Co-Cr-Fe-Mn-Ni high entropy alloy system, 75 (2016) 15–24. doi:10.1016/j.intermet.2016.04.007.

[32] S. Yang, X. Yan, K. Yang, Z. Fu, Effect of the addition of nano-Al2O3 on the microstructure and mechanical properties of twinned Al0.4FeCrCoNi1.2Ti0.3 alloys, 131 (2016) 69–72. doi:10.1016/j.vacuum.2016.05.019.

[33] Y.F. Ye, Q. Wang, Y.L. Zhao, Q.F. He, J. Lu, Y. Yang, Elemental segregation in solid-solution high-entropy alloys: experiments and modeling, J. Alloys Compd. 681 (2016) 167–174, http://dx.doi.org/10.1016/j.jallcom.2016.04.239.

[34] H. Yuan, M.H. Tsai, G. Sha, F. Liu, Z. Horita, Y. Zhu, J.T. Wang, Atomic-scale homogenization in an fcc-based high-entropy alloy via severe plastic deformation, 686 (2016) 15–23. doi:10.1016/j.jallcom.2016.05.337.

[35] S. Zhang, C.L. Wu, C.H. Zhang, M. Guan, J.Z. Tan, Laser surface alloying of FeCoCrAlNi high-entropy alloy on 304 stainless steel to enhance corrosion and cavitation erosion resistance, Opt. Laser Technol. 84 (2016) 23–31, http://dx.doi.org/10.1016/j.optlastec.2016.04.011.

[36] Y. Zhang, Y. Liu, Y. Li, X. Chen, H. Zhang, Microstructure and mechanical properties of a refractory HfNbTiVSi0.5 high-entropy alloy composite, Mater. Lett. 174 (2016) 82–85, http://dx.doi.org/10.1016/j.matlet.2016.03.092.

[37] Y.J. Zhao, J.W. Qiao, S.G. Ma, M.C. Gao, H.J. Yang, M.W. Chen, Y. Zhang, A hexagonal close-packed high-entropy alloy: the effect of entropy, Mater. Des. 96 (2016) 10–15, http://dx.doi.org/10.1016/j.matdes.2016.01.149.

[38] O.N. Senkov, D. Isheim, D.N. Seidman, A.L. Pilchak, Development of a refractory high entropy superalloy, 18 (2016). doi:10.3390/e18030102.

[39] O.N. Senkov, D.B. Miracle, A new thermodynamic parameter to predict formation of solid solution or intermetallic phases in high entropy alloys, 658 (2016) 603–607. doi:10.1016/j.jallcom.2015.10.279.

[40] J.Y. He, H. Wang, H.L. Huang, X.D. Xu, M.W. Chen, Y. Wu, X.J. Liu, T.G. Nieh, K. An, Z.P. Lu, A precipitation-hardened high-entropy alloy with outstanding tensile properties, 102 (2016) 187–196. doi:10.1016/j.actamat.2015.08.076.

[41] L.R. Shaginyan, V.F. Gorban', N.A. Krapivka, S.A. Firstov, I.F. Kopylov, Properties of coatings of the Al–Cr–Fe–Co–Ni–Cu–V high entropy alloy produced by the magnetron sputtering, 38 (2016) 25–33. doi:10.3103/S1063457616010044.

[42] R. Carroll, C. Lee, C.W. Tsai, J.W. Yeh, J. Antonaglia, B.A.W. Brinkman, M. Leblanc, X. Xie, S. Chen, P.K. Liaw, K.A. Dahmen, Experiments and model for serration statistics in low-entropy, medium-entropy, and high-entropy alloys, 5 (2015). doi:10.1038/srep16997.

[43] M. Caro, L.K. Béland, G.D. Samolyuk, R.E. Stoller, A. Caro, Lattice thermal conductivity of multi-component alloys, 648 (2015) 408–413. doi:10.1016/j.jallcom.2015.06.035.

[44] Y. Zou, H. Ma, R. Spolenak, Ultrastrong ductile and stable high-entropy alloys at small scales, Nat. Commun. 6 (2015) 7748, http://dx.doi.org/10.1038/ncomms8748.

[45] P. Singh, A. V. Smirnov, D.D. Johnson, Atomic short-range order and incipient long-range order in high-entropy alloys, 91 (2015). doi:10.1103/PhysRevB.91.224204.

[46] A.D. Pogrebnjak, I.V. Yakushchenko, O.V. Bondar, O.V. Sobol', V.M. Beresnev, K. Oyoshi, H. Amekura, Y. Takeda, Influence of implantation of Au– ions on the microstructure and mechanical properties of the nanostructured multielement (TiZrHf VNbTa)N coating, Phys. Solid State 57 (2015) 1559–1564, http://dx.doi.org/10.1134/S1063783415080259.

[47] X. Feng, G. Tang, X. Ma, M. Sun, L. Wang, Characteristics of multi-element (ZrTaNbTiW)N films prepared by magnetron sputtering and plasma based ion implantation, Nucl. Instrum. Methods Phys. Res. Sec. B 301 (2013) 29–35, http://dx.doi.org/10.1016/j.nimb.2013.03.001.

[48] V.V. Uglov, G. Abadias, A.Y. Rovbut, S.V. Zlotski, I.A. Saladukhin, V.A. Skuratov, S. Petrovich, Thermal stability of nanocrystalline (Ti, Zr)0.54Al0.46N films implanted by He+ ions, 354 (2015) 269–273. doi:10.1016/j.nimb.2014.11.012.

[49] F.F. Komarov, A.D. Pogrebnyak, S.V. Konstantinov, Physics of nanostructures at]radiation resistance of high-entropy nanostructured (Ti, Hf, Zr, V, Nb)N coatings, 60 (2015) 1519–1524. doi:10.1134/S1063784215100187.

[50] L.S. Metlov, M.M. Myshlyaev, A.V. Khomenko, I.A. Lyashenko, A model of grain boundary sliding during deformation, Tech. Phys. Lett. 38 (2012) 972–974, http://dx.doi.org/10.1134/S1063785012110107.

[51] S. Abhaya, R. Rajaraman, S. Kalavathi, C. David, B.K. Panigrahi, G. Amarendra, Effect of dose and post irradiation annealing in Ni implanted high entropy alloy FeCrCoNi using slow positron beam, J. Alloys Compd. 669 (2016) 117–122, http://dx.doi.org/10.1016/j.jallcom.2016.01.242.

[52] X. Yi, M.L. Jenkins, K. Hattar, P.D. Edmondson, S.G. Roberts, Characterisation of radiation damage in W and W-based alloys from 2 MeV self-ion near-bulk implantations, Acta Mater. 92 (2015) 163–177, http://dx.doi.org/10.1016/j.actamat.2015.04.015.

[53] X. Obradović, D. Pjević, A. Peruško, A. Grce, M. Milosavljević, K.P. Homewood, Z. Siketić, Effects of Helium Ion Irradiation on Bubble Formation in AlN/TiN Multilayered System, Elsevier, 2015, http://dx.doi.org/10.1016/j.tsf.2015.03.074, pp. 164–168.

[54] A.D. Pogrebnjak, I.V. Yakushchenko, O.V. Bondar, O.V. Sobol', V.M. Beresnev, K. Oyoshi, H. Amekura, Y. Takeda, The microstructure of a multielement nanostructured (TiZrHfVNbTa)N coating and its resistance to irradiation with Au– ions, Tech. Phys. Lett. 41 (2015) 1054–1057, http://dx.doi.org/10.1134/S1063785015110085.

[55] A.D. Pogrebnjak, I.V. Yakushchenko, O.V. Bondar, V.M. Beresnev, K. Oyoshi, O.M. Ivasishin, H. Amekura, Y. Takeda, M. Opielak, C. Kozak, Irradiation resistance, microstructure and mechanical properties of nanostructured (TiZrHfVNbTa)N coatings, J. Alloys Compd. 679 (2016) 155–163, http://dx.doi.org/10.1016/j.jallcom.2016.04.064.

[56] A.D. Pogrebnjak, D. Eyidi, G. Abadias, O.V. Bondar, V.M. Beresnev, O.V. Sobol, Structure and properties of arc evaporated nanoscale TiN/MoN multilayered systems, Int. J. Refract. Met. Hard Mater. 48 (2015) 222–228, http://dx.doi.org/10.1016/j.ijrmhm.2014.07.043.

[57] L.C. Feldman, J.W. Mayer, Fundamentals of surface and thin film analysis, North-Holland, 1986. <https://books.google.com/books?id=wDdRAAAAMAAJ&pgis=1>.

[58] U. Welzel, J. Ligot, P. Lamparter, A.C. Vermeulen, E.J. Mittemeijer, Stress analysis of polycrystalline thin films and surface regions by X-ray diffraction, J. Appl. Crystallogr. 38 (2005) 1–29, http://dx.doi.org/10.1107/S0021889804029516.

[59] G. Abadias, Stress and preferred orientation in nitride-based PVD coatings, Surf. Coatings Technol. 202 (2008) 2223–2235, http://dx.doi.org/10.1016/j.surfcoat.2007.08.029.

[60] P. Giannozzi, S. Baroni, N. Bonini, M. Calandra, R. Car, C. Cavazzoni, D. Ceresoli, G.L. Chiarotti, M. Cococcioni, I. Dabo, A. Dal Corso, S. de Gironcoli, S. Fabris, G. Fratesi, R. Gebauer, U. Gerstmann, C. Gougoussis, A. Kokalj, M. Lazzeri, L. Martin-Samos, N. Marzari, F. Mauri, R. Mazzarello, S. Paolini, A. Pasquarello, L. Paulatto, C. Sbraccia, S. Scandolo, G. Sclauzero, A.P. Seitsonen, A. Smogunov, P. Umari, R.M. Wentzcovitch, QUANTUM ESPRESSO: a modular and open-source software project for quantum simulations of materials, J. Phys.: Condens. Matter 21 (2009) 395502, http://dx.doi.org/10.1088/0953-8984/21/39/395502.

[61] D. Vanderbilt, Soft self-consistent pseudopotentials in a generalized eigenvalue formalism, Phys. Rev. B. 41 (1990) 7892–7895, http://dx.doi.org/10.1103/PhysRevB.41.7892.

[62] J.P. Perdew, K. Burke, M. Ernzerhof, Generalized gradient approximation made simple, Phys. Rev. Lett. 77 (1996) 3865–3868.

[63] S.R. Billeter, A. Curioni, W. Andreoni, Efficient linear scaling geometry optimization and transition-state search for direct wavefunction optimization schemes in density functional theory using a plane-wave basis, Comput. Mater. Sci. 27 (2003) 437–445, http://dx.doi.org/10.1016/S0927-0256(03)00043-0.

[64] G. Abadias, M.B. Kanoun, S. Goumri-Said, L. Koutsokeras, S.N. Dub, P. Djemia, Electronic structure and mechanical properties of ternary ZrTaN alloys studied by ab initio calculations and thin-film growth experiments, Phys. Rev. B. 90 (2014) 144107, http://dx.doi.org/10.1103/PhysRevB.90.144107.

[65] S.M. Duvanov, A.G. Balogh, Two-stage diffusion and nanoparticle formation in heavily implanted polycrystalline Al2O3, Nucl. Instrum. Methods Phys. Res. Sect. B 171 (2000) 475–480, http://dx.doi.org/10.1016/S0168-583X(00)00320-7.

[66] M. Mayer, RESOLNRA: a new program for optimizing the achievable depth resolution of ion beam analysis methods, Nucl. Instrum. Methods Phys. Res. Sect. B 266 (2008) 1852–1857, http://dx.doi.org/10.1016/j.nimb.2007.11.071.

[67] M. Mayer, SIMNRA User's Guide Report IPP 9/113, Garching, Germany, 1997.